Catalysis Letters
https://doi.org/10.1007/s10562-024-04820-w

Impact of M (M = Co, Cu, Fe, Zr) Doping on CeO_2-Based Catalysts for Ammonia Selective Catalytic Oxidation at Low Temperatures

Longwei Cheng[1] · Pan Wang[1] · Quanxin Ye[1] · Hongyu Zhao[1] · Sheikh Muhammad Farhan[1] · Tong Yan[1] · Hailin Zhao[2]

Received: 7 July 2024 / Accepted: 28 August 2024

Abstract

Selective catalytic conversion of ammonia to nitrogen is an effective method for reducing ammonia emissions from both stationary and mobile sources. In this study, CeO_2-based catalysts (M/CeO_2, M = Co, Cu, Fe, Zr) were synthesized using the sol–gel method and subsequently tested on a simulated gas experimental platform to assess their performance in NH_3 selective catalytic oxidation (NH_3-SCO). Results showed that Co/CeO_2 and Cu/CeO_2 catalysts exhibited high ammonia oxidation activity at respectively low temperatures, with T_{50} 196.8 and 229.5 °C, and T_{90} 239.2 and 292.1 °C. However, it was observed that while Co/CeO_2 displayed poor N_2 selectivity, Cu/CeO_2 demonstrated good N_2 selectivity. The superior catalytic performance of Cu/CeO_2 and Co/CeO_2 catalysts compared to Fe/CeO_2 and Zr/CeO_2 can be attributed to their distinct interactions with Ce. Subsequent characterization experiments were conducted to elucidate these interactions. BET and SEM analyses revealed that all M/CeO_2 catalysts possessed a typical mesoporous structure. XRD and XPS results indicated that the primary phase of each catalyst was CeO_2, and the incorporation of M transition metals did not alter the cubic fluorite structure. The interaction between the M metal and Ce varied, impacting the Ce^{3+} content on the catalyst surface, which in turn influenced oxygen species adsorption and ammonia oxidation activity. H_2-TPR and Raman spectroscopy analyses demonstrated that M metal incorporation shifted the CeO_2 reduction peak, thereby altering reduction properties and affecting oxidation performance. In particular, the Co-metal composite shifted the reduction peak to a lower temperature, thereby enhancing the reduction properties and indirectly increasing oxidation activity.

Graphical Abstract

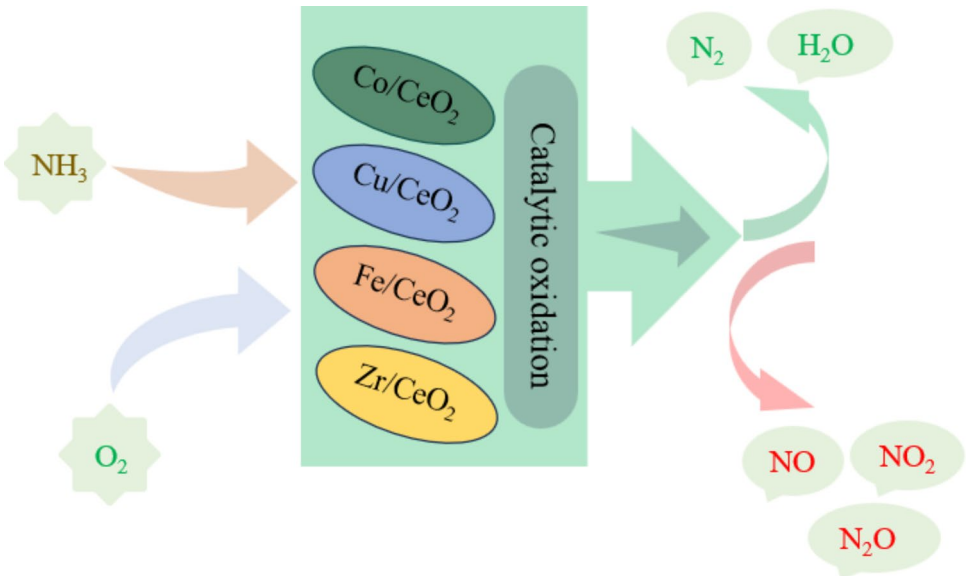

Extended author information available on the last page of the article

Published online: 16 September 2024

Keywords Ammonia · Selective catalytic oxidation · CeO_2-based catalysts · N_2 selectivity · Synergistic interaction

1 Introduction

As a critical sector for carbon reduction, the transportation industry holds significant responsibility in implementing the dual-carbon strategy. The replacement of traditional petroleum fuels with zero-carbon fuels plays a key role in this process. The development and popularization of ammonia-fueled engines is a good choice for the use of zero-carbon fuels. Undoubtedly, the use of ammonia as a fuel for engines has the potential to significantly decrease CO_2 emissions and serves as a robust foundation for the dual-carbon approach. However, the issue of hazardous ammonia emissions that arise from engine fuel leakage and incomplete fuel combustion under special operating conditions must be resolved. Ammonia is a colorless gas with a strong odor at room temperature and pressure and is the most abundant alkaline gas in the atmosphere. It significantly contributes to haze formation by reacting with gaseous nitric acid and sulfuric acid in the air, producing ammonium sulfate, ammonium nitrate, and other secondary particulate matter. These secondary particulate matters account for 50–70% of the PM2.5 content [1, 2]. Exposure to ammonia concentrations above 500 ppm, can cause eye irritation, and lungs diseases; while levels higher than 10,000 ppm are potentially fatal [3]. Due to the significant risk ammonia poses to the environment and human beings, the management of hazardous ammonia has increasingly attracted extensive attention from society and scholars.

Several techniques have been developed for the management of hazardous ammonia emissions., mainly including absorption decomposition [4], biofiltration [5], catalytic decomposition [6], and selective catalytic oxidation [7–10]. The absorption decomposition method uses acidic solutions such as HNO_3 or H_2SO_4 to adsorb alkaline NH_3 through acid–base neutralization; the biofiltration method uses the growth and metabolism of microorganisms to decompose NH_3 in a specific reaction vessel; catalytic decomposition is the direct decomposition of NH_3 into N_2 and H_2 at high temperature, which is the reverse reaction of ammonia synthesis; selective catalytic oxidation is the use of catalysts to convert NH_3 into N_2 and H_2O in a directional manner. Among them, NH_3-SCO is considered to be the most effective treatment process for mitigating harmful ammonia emissions from the exhaust of stationary industrial and mobile sources and the main reaction equations are as follows [11]:

$$4NH_3 + 3O_2 \rightarrow 2N_2 + 6H_2O \quad (1)$$

$$4NH_3 + 5O_2 \rightarrow 4NO + 6H_2O \quad (2)$$

$$4NH_3 + 7O_2 \rightarrow NO_2 + 6H_2O \quad (3)$$

$$2NH_3 + 2O_2 \rightarrow N_2O + 3H_2O \quad (4)$$

The reaction pathway outlined in the process (1) is the most effective method for reducing ammonia pollution. Conversely, processes (2)–(4) involve peroxide side reactions that generate environmentally harmful NO_x byproducts, which should be minimized. The catalyst, which is fundamental to the NH_3-SCO process, is crucial in determining the efficiency and selectivity of the desired reaction pathway. According to the classification of the main active site, the current mainstream NH_3-SCO catalysts are mainly divided into two categories: noble metal catalysts and transition metal oxide catalysts. Scholars have conducted extensive research on precious metals mainly including Pt, Pd, Ru, Au, and Ir [12–15], which have excellent catalytic activity and stability for the ammonia oxidation reaction process at low temperatures. However, the shortcomings are the high cost of precious metal catalysts and the challenge of low N_2 selectivity due to peroxidation, which severely limit their wide application. Therefore, researchers have shifted their focus to transition metal oxides, including MoO_3, CuO, CeO_2, Fe_2O_3, TiO_2, Co_3O_4, and MnO_2 [16–22]. Transition metal oxidation catalysts are generally more N_2 selective and more abundant at relatively low costs compared to noble metal-based catalysts, although they exhibit lower activity. The ideal catalyst would combine the advantages of both, with high catalytic activity and N_2 selectivity for ammonia oxidation. CeO_2, a rare earth oxide, is well-known for its abundant oxygen vacancies, excellent redox capacity, and effective oxygen storage and release capabilities, owing to the facile transition between Ce^{3+} and Ce^{4+} ions. Additionally, CeO_2 exhibits strong interactions with other metals. These interactions enable the development of high-performance composite oxide NH_3-SCO catalysts when CeO_2 is combined with a second metal oxide (MO_x), despite pure CeO_2 having weak NH_3 oxidation activity [23]. Transition metal elements such as Co, Cu, Fe, and Zr are considered cost-effective alternatives to precious metals. Among these, Co, Cu, and Fe catalysts exhibit favorable redox properties and catalytic activity, making them extensively utilized in environmental catalysis applications, including NOx selective catalytic reduction, CO oxidation, water vapor

shift reaction, and VOC oxidation reaction. Zr is recognized for its exceptional thermal stability, and catalysts incorporating Zr are known for their stability and oxygen storage capabilities. Therefore, exploring the synergistic effects of these four elements in conjunction with CeO_2 to develop novel catalysts for NH_3-SCO holds significant research potential.

In this research, M metals (M = Co, Cu, Fe, Zr) were integrated into CeO_2 using the sol–gel method to achieve a composite oxide catalyst with excellent ammonia oxidation performance and high N_2 selectivity. Subsequently, the simulation gas experiments were carried out to evaluate the catalytic performance of CeO_2-based catalysts. Furthermore, a series of characterization methods such as BET, SEM, XRD, XPS, H_2-TPR, and Raman were employed to analyze the physicochemical properties and explain the effects of the strong interactions between Ce and the metals.

2 Experimental

2.1 Catalyst Preparation

A series of M/CeO_2 (M = Co, Cu, Fe, Zr) catalyst samples were prepared using the sol–gel method. Taking Co/ CeO_2 as an example, the specific preparation steps were as follows: 40 g of Ce-Co mixed-oxide powders were targeted. The nitrate precursors, cobalt nitrate ($Co(NO_3)_2{\cdot}6H_2O$) and cerium nitrate ($Ce(NO_3)_3{\cdot}6H_2O$), were mixed in a 1:1 molar ratio. Both nitrates were dissolved in 150 ml of deionized water with magnetic stirring for 1 h. Subsequently, the complexing agent citric acid monohydrate ($C_6H_8O_7{\cdot}H_2O$) was slowly added. The amount of $C_6H_8O_7{\cdot}H_2O$ required was determined based on the valence and quantity of the nitrate precursors, calculated as follows: the molar amount of $C_6H_8O_7{\cdot}H_2O = (Co^{2+} \times 2 + Ce^{3+} \times 3) \times 1.1$ (the factor 1.1 ensures complete complexation). After the citric acid addition, the solution was stirred for an additional hour, then transferred to a water bath at 80 °C and heated for 3–5 h with continuous stirring until a viscous gel was formed. The obtained gel was then dried in a constant temperature oven at 110 °C for 24 h to form a spongy substance and then calcined at 400 °C for 3 h to burn off nitrate and carbon species to obtain the finished catalyst sample powder. Finally, a portion of the powder was added with water and binder to adjust the viscosity then coated onto cordierite using a vacuum coater, and then roasted at 400 °C for 3 h to obtain a complete catalyst sample Co/CeO_2 that could be tested; the rest of the catalyst powder was retained for characterization. Cu/CeO_2, Fe/CeO_2, and Zr/CeO_2 catalyst samples were produced in the same way.

2.2 Catalysts Characterization

2.2.1 N_2 Adsorption/Desorption

The structural characteristics of the catalyst samples, such as specific surface area, pore volume, and pore size, were determined on a JW-BK200B physical adsorption tester (Beijing Jingwei Gao Bo). The pretreatment conditions were: vacuum, 300 °C, 3 h; the testing conditions were: high purity N_2 adsorption and desorption. The specific surface area of the samples was calculated by BET (Brunner-Emmett-Teller) equation, and the pore volume pore size, etc. were calculated by BJH (Barret–Joyner–Halenda) analysis.

2.2.2 SEM

The samples were imaged by scanning electron microscopy using a JEOL JSM-6301F scanning electron microscope with a magnification level of 500 nm.

2.2.3 XRD

The crystalline structure analysis of the samples was carried out on a Smart lab SE-type X-ray diffractometer, using Cu Ka rays as the ray source ($\lambda = 0.15406$). Test conditions: operating voltage 40 kV, operating current 40 mA; signal acquisition resolution 0.02°/step, scanning speed 5°/min, 2θ range 10°-90°.

2.2.4 XPS

X-ray photoelectron spectroscopy was performed on a Kratos AXIS-Ultra DLD under ultra-high vacuum at 10^{-9} Pa with Al-Kα radiation as the source (voltage: 15 kV; power: 250 W) and an analytical range of 0–5000 eV. All data were calibrated to a C 1 s binding energy of 284.8 eV. Standard for calibration.

2.2.5 H_2-TPR

H_2-temperature programmed reduction (H_2-TPR) experiments were carried out on a fully automated chemisorption instrument, Auto Chem II 2920, equipped with a thermal conductivity detector (TCD). The catalyst sample powder (50 mg) was pretreated in a pure He gas stream at a gas flow rate of 50 ml/min and a temperature of 350 °C for 30 min. After that, the temperature was lowered to 40 °C, and the powder was heated up to 800 °C in a 10 vol% H_2/He gas stream at a temperature rise rate of 10 °C/min, and the change of the signal was detected and recorded by the TCD.

2.2.6 Raman

The instrument used for Raman testing was a Thermo Scientific DXR micro-spectrometer. A He–Cd laser with a wavelength of 532 nm was used for excitation and the power was 3 mW.

2.3 Catalytic Activity Tests

The NH_3 oxidation performance of the M/CeO_2 catalyst was evaluated using a fixed-bed flow reactor. The fixed-bed flow reactor mainly consists of three parts: an inlet air system, catalytic reaction system, and data acquisition system, as shown in Fig. 1.

Experimental procedures involved wrapping the catalyst-coated cordierite with quartz cotton and placing it in a heating furnace, forming a cylinder (50 cm length, 24 cm diameter). Gas flow rates were regulated before entering the reaction gas path to stabilize components. A temperature sensor, positioned 0.5–1 cm ahead of the catalyst, monitored real-time gas temperature. Inlet gas contained 500 ppm NH_3 and 8% O_2, with N_2 as the equilibrium gas. Gas hourly space velocity (GHSV) was maintained at 40,000 h^{-1}, with reactions occurring at temperatures ranging from 100 to 600 °C. NO_x, N_2O, and NH_3 concentrations in exhaust gas were analyzed using an FTIR gas analyzer (MKS). In this study, NH_3 conversion and N_2 selectivity were calculated by the following formulas:

$$NH_3\ \text{conversion}(\%) = \left(\frac{\left[NH_3 \right]_{in} - \left[NH_3 \right]_{out}}{\left[NH_3 \right]_{in}} \right) \times 100 \tag{5}$$

$$N_2\ \text{selectivity}(\%) = \left(\frac{\left[NH_3 \right]_{in} - \left[NH_3 \right]_{out} - \left[NO \right]_{out} - \left[NO_2 \right]_{out} - 2\left[N_2O \right]_{out}}{\left[NH_3 \right]_{in} - \left[NH_3 \right]_{out}} \right) \times 100 \tag{6}$$

3 Results and Discussion

3.1 Catalytic Activity

A comprehensive evaluation of the catalytic performance of M/CeO_2 (M = Co, Cu, Fe, Zr) catalysts in the selective catalytic oxidation of ammonia as a function of temperature was carried out, and the results are shown in Fig. 2. Notably all four catalyst samples, Co/CeO_2, Cu/CeO_2, Fe/CeO_2, and Zr/CeO_2, exhibited good ammonia oxidation activities, with T_{50} of 196.8, 229.5, 283.7, and 313.5 °C, respectively, and T_{90} of 239.2, 292.1, 373.7, and 416.3 °C,

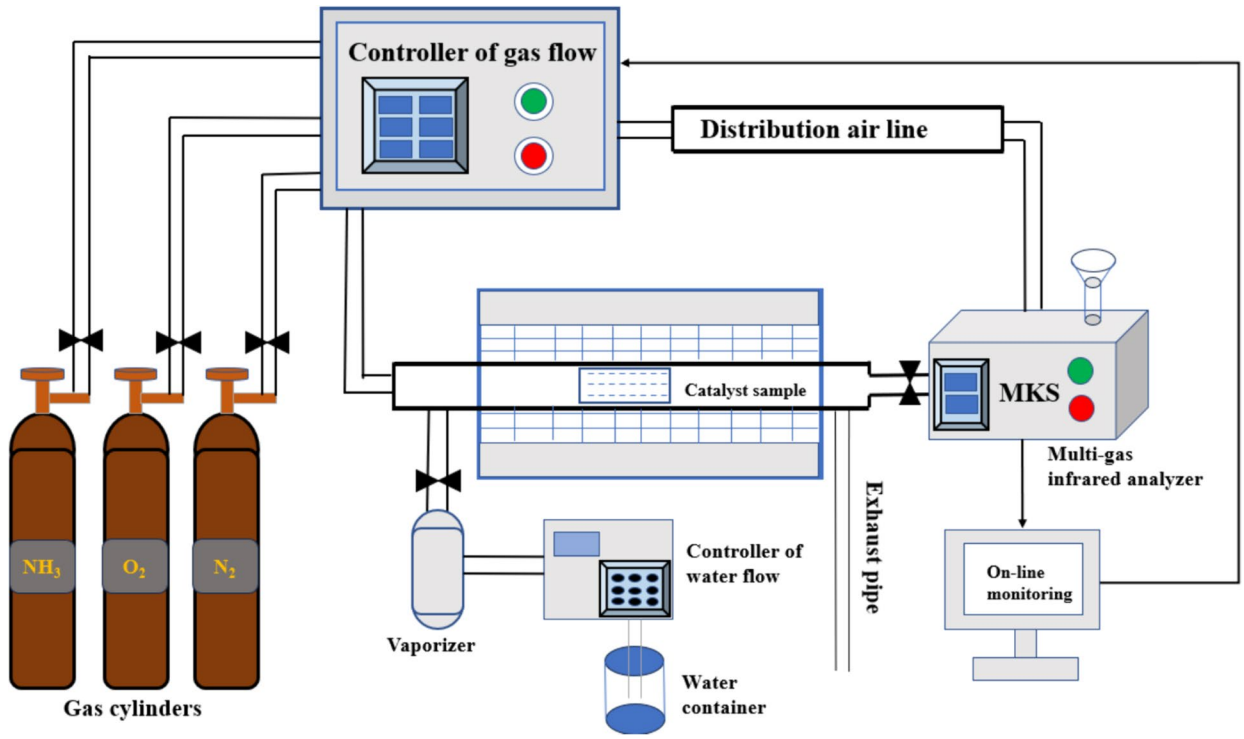

Fig. 1 Experimental platform of fixed-bed reactor

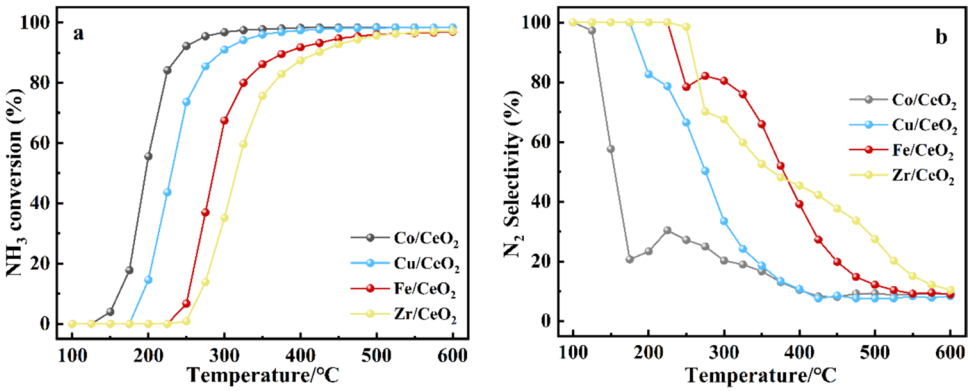

Fig. 2 Ammonia oxidation activity of M/CeO_2 (M = Co, Cu, Fe, Zr) catalysts: **a** NH_3 conversion, **b** N_2 selectivity

respectively. Over a wide range of temperatures, different catalysts converted ammonia to nitrogen at different rates and produced different reaction by-products. Relative to other catalyst types, Zr/CeO_2 has lower catalytic activity, shows no ammonia reaction below 250 °C, and has greater T_{50} and T_{90} values as depicted in Fig. 2a. At 250 °C, however, Co/CeO_2 had exceptional catalytic activity, almost completely converting ammonia. A general order of total ammonia conversion over M/CeO_2 catalysts was found to be as follows: $Co/CeO_2 > Cu/CeO_2 > Fe/CeO_2 > Zr/CeO_2$.

As can be seen from Fig. 2b, there is a trend of decreasing N_2 selectivity with increasing reaction temperature for all catalyst samples. The N_2 selectivity of ammonia oxidation over M/CeO_2 catalysts is ranked as $Co/CeO_2 < Cu/CeO_2 < Fe/CeO_2 < Zr/CeO_2$. The results revealed an inverse relationship between ammonia conversion activity and N_2 selectivity in the catalyst samples. Higher ammonia conversion activity resulted in lower N_2 selectivity, while lower ammonia conversion activity enhanced N_2 selectivity. Among the four catalysts studied, Cu/CeO_2 exhibited the most balanced performance, achieving both high ammonia conversion and favorable N_2 selectivity. This optimal performance was attributed to the distinct synergistic effects between the copper and cerium oxide components.

3.2 Catalyst Characterization

3.2.1 BET Analysis

Figure 3a shows the N_2 adsorption/desorption isotherms for the M/CeO_2 (M = Co, Cu, Fe, Zr) given in Fig. 3a, used to determine their specific surface area and pore structure. From the adsorption and desorption curves of nitrogen, all the samples exhibit similar isothermal curves i.e. type IV isotherms. The hysteresis loops are all in the relative pressure (P/P_0) range of 0.4–1.0 and are classified as H3 hysteresis by IUPAC classification, indicating a slit-like pore structure due to the aggregation of lamellar particles. The pore size distribution of each sample was determined by the BJH method, as shown in Fig. 3b, ranging from 3 to 16 nm, within the mesopore size (2–50 nm). This confirms that all the samples exhibit typical mesoporous structures. Among the catalysts, Fe/CeO_2 catalyst demonstrated broad pore size distribution, while Co/CeO_2, Cu/CeO_2, and Zr/CeO_2, had narrower, similar pore size distribution ranges. The corresponding specific surface area, pore size, and pore volume of each catalyst sample are detailed in Table 1. The superior ammonia oxidation capabilities of Co/CeO_2 could be attributed to its optimized surface areas, while the good performance of Cu/CeO_2 may be linked to its minimal aperture.

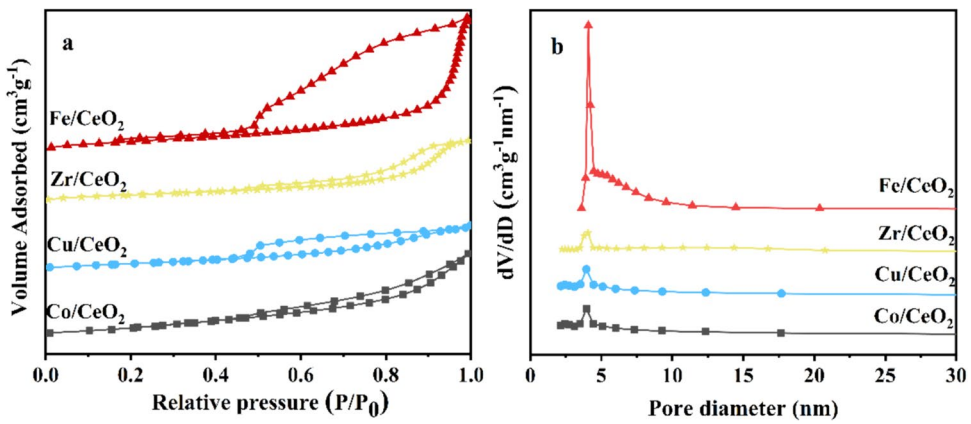

Fig. 3 **a** N_2 adsorption/desorption isotherms and **b** the corresponding pore size distribution curves of M/CeO_2 (M = Co, Cu, Zr, Fe)

Table 1 Pore structure parameters of prepared samples

Sample	S_{BET}[a] (m^2g^{-1})	V_{BJH}[b] (cm^3g^{-1})	D_{BJH}[c] (nm)
Co/CeO_2	77.37	0.23	7.43
Cu/CeO_2	55.53	0.13	4.40
Fe/CeO_2	73.97	0.40	5.60
Zr/CeO_2	56.80	0.16	10.41

[a]BET surface area

[b]BJH desorption cumulative pore volume

[c]BJH desorption average pore diameter

In contrast, the reduced performance of Zr/CeO_2 could be ascribed to its limited surface area and high pore size.

3.2.2 SEM Analysis

Figure 4a-d shows the scanning electron micrographs of M/CeO_2 (M = Co, Cu, Fe, Zr) catalysts synthesized by the citric acid sol–gel method. Due to the high viscosity of the sol–gel, the surface of all the samples was not regular and showed aggregates with disordered shapes, which somewhat reduced the dispersion of the particles [24]. Figure 4a illustrates that the surface of the Co/CeO_2 is notably rough, characterized by numerous protrusions, depressions, and a substantial number of aggregates. This observation is consistent with the data presented in Table 1, which indicates that Co/CeO_2 possesses the largest specific surface area. A larger specific surface area can expose more active sites, potentially enhancing the adsorption and conversion of NH_3, thereby improving the efficiency of ammonia oxidation. [25], this also corresponds to the best ammonia oxidation activity of the Co/CeO_2 sample in Fig. 2a. In Fig. 4c, the Cu/CeO_2 sample shows a disseminated shape with a high number of pores, but not many particles are distributed on the surface, possibly due to the mosaic inside a large number of pores. The Fe/CeO_2 and Zr/CeO_2 samples in Fig. 4b, d are relatively smooth, with more rounded and sparse pores. This indicates that these two samples exhibit easier sintering during the preparation process, consistent with the observed lower ammonia oxidation activity presented in Fig. 2a.

3.2.3 XRD Analysis

To investigate the physical phases of M/CeO_2 (M = Co, Cu, Fe, Zr), wide-angle XRD tests were conducted. Figure 5 shows the XRD spectra for the Co/CeO_2, Cu/CeO_2, Fe/CeO_2, and Zr/CeO_2 produced after roasting at 400 °C. From the

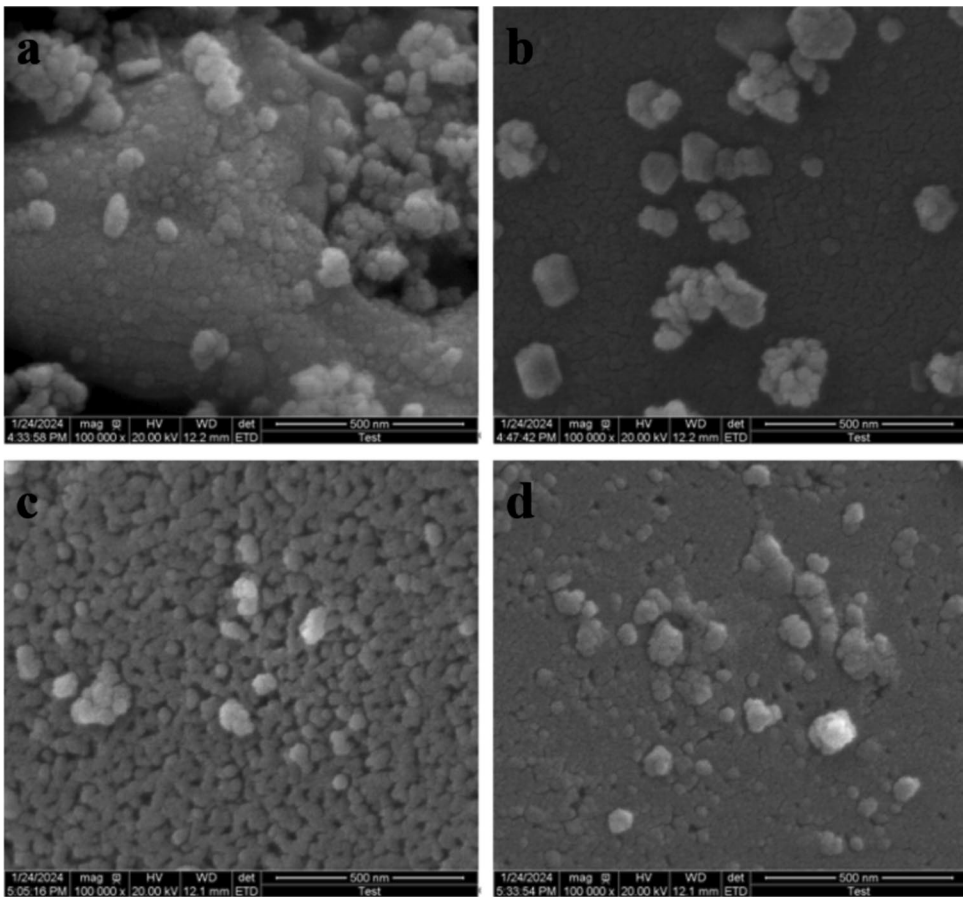

Fig. 4 Scanning electron micrographs of the four catalyst samples: **a** Co/CeO_2, **b** Fe/CeO_2, **c** Cu/CeO_2, **d** Zr/CeO_2

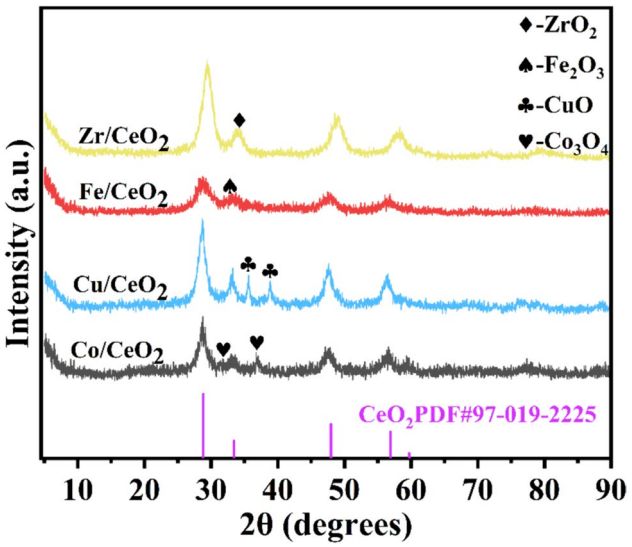

Fig. 5 XRD spectra of four catalyst samples of M/CeO_2 (M = Co, Cu, Fe, Zr)

figure, it can be seen that the above catalysts show XRD diffraction peaks around 2θ = 28.83°, 33.41°, 47.97°, 56.93°, 59.71°, and their diffraction peak positions are in agreement with the standard card of CeO_2 (PDF#97–019-2225). The study reveals CeO_2 as the primary phase among the catalysts examined, maintaining its cubic fluorite structure i.e., face-centered cubic structure, even after incorporating transition metals (M = Co, Cu, Fe, Zr) via the citric acid sol–gel method. Only minor characteristic peaks corresponding to Fe_2O_3 and ZrO_2 were observed in the XRD spectra of the Fe/CeO_2 and Zr/CeO_2 samples, suggesting a homogeneous distribution of Fe and Zr species on the surface of the catalyst. Analysis of the Cu/CeO_2 spectrum revealed distinct characteristic diffraction peaks observed at 2θ = 35.6° and 38.8°, which could be attributed to CuO (PDF#00-005-0661), suggesting that aggregation and crystallization of certain CuO species taking place on the catalyst surface. For the Co/CeO_2 catalyst sample, characteristic diffraction peaks were observed at 2θ = 31.7° and 36.8°, corresponding to Co_3O_4 (PDF#04-005-4386), suggesting that the Co species were not uniformly dispersed on the catalyst surface.

3.2.4 XPS Analysis

The XPS results of M/CeO_2 (M = Co, Cu, Fe, Zr) are shown in Fig. 6, while Table 2 shows the elemental and atomic ratios of each catalyst. XPS analysis effectively characterizes the valence states of active substances present on the surface of the catalyst and quantifies the atomics distribution. The XPS profiles of M (M = Co, Cu, Fe, Zr) are shown in Fig. 6a. In the case of Co, the high-resolution Co 2p spectrum reveals two prominent peaks at roughly 780.0 and 795.5 eV which corresponds to Co $2p_{3/2}$ and Co $2p_{1/2}$, respectively. In addition, the characteristic satellite peaks of Co oxides such as Co_3O_4, Co_2O_3, and CoO can be observed at the position around 786 eV [26]. It is clear that the specific valence state of the cobalt ion cannot be determined from the main peak

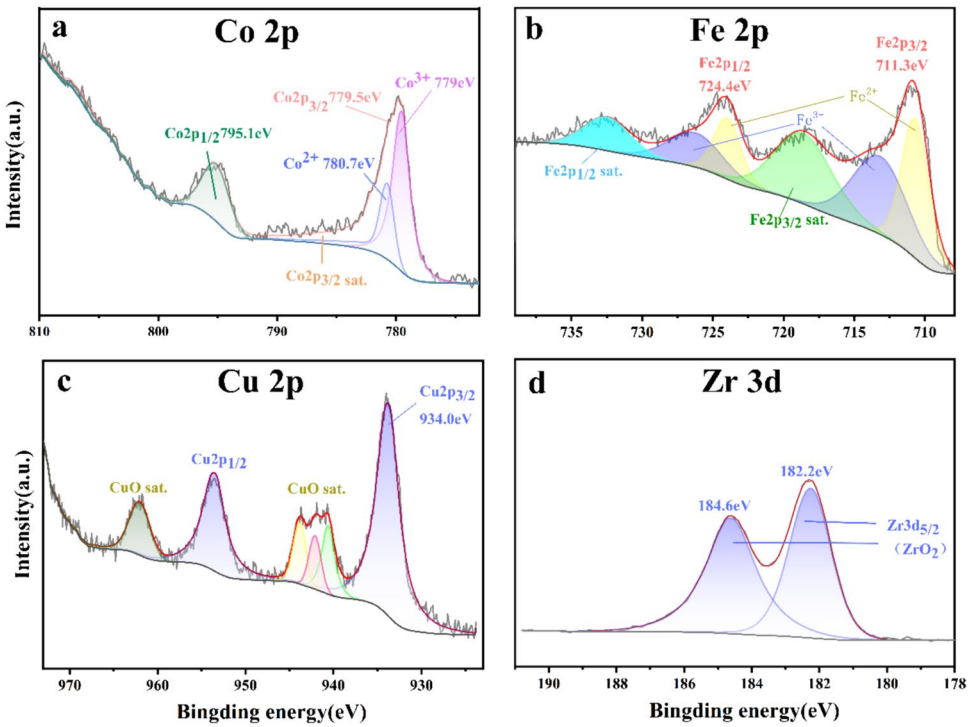

Fig. 6 XPS profiles of M: **a** Co 2p, **b** Fe 2p, **c** Cu 2p, **d** Zr 3d

Table 2 XPS data for different M/CeO_2 (M = Co, Cu, Fe, Zr) catalysts: surface atomic concentration of M, Ce, O, and valence distribution of elements

Catalysts	Surface atomic ratio (%)			Ce^{3+}/Ce^{4+}	O_β/O	O_γ/O
	M	Ce	O			
Co/CeO_2	3.77	21.58	74.65	0.29	0.19	0.15
Cu/CeO_2	24	14.91	61.09	0.18	0.23	0.12
Fe/CeO_2	14.5	14.34	71.16	0.14	0.26	0.09
Zr/CeO_2	6.05	5.25	88.70	0.12	0.29	0.06

alone and needs to be confirmed in combination with the satellite peaks. A strong oscillatory satellite peak belonging to paramagnetic Co^{2+} was observed around 786 eV, which is 6 eV higher than the binding energy of Co $2p_{3/2}$, the antimagnetic low-spin Co^{3+} lacks such an oscillatory peak [27]. By comparing the ratio of peak intensities between the oscillatory peak and the main peak, an approximate assessment of the Co^{2+} content can be inferred.

The spectral results of Fe 2p of the Fe/CeO_2 catalyst samples are shown in Fig. 6b. The primary peaks of Fe $2p_{3/2}$ and Fe $2p_{1/2}$, with binding energies approximately at 711.3 and 724.4 eV, respectively, can be deconvoluted into two distinct peaks corresponding to the characteristic signals of Fe^{2+} and Fe^{3+}. This observation indicates that Fe^{2+} and Fe^{3+} coexist on the surface of the synthesized Fe/CeO_2 catalyst samples. The relative concentrations of Fe^{2+} and Fe^{3+} can be determined from the characteristic peak areas. Previous studies [28] have noted that the presence of Ce on the catalyst surface can increase the Fe^{2+} content. This is likely due to the synergistic interaction between Fe and Ce, which facilitates the redox equilibrium of $Fe^{3+} + Ce^{3+} \leftrightarrow Fe^{2+} + Ce^{4+}$. Figure 6c depicts the Cu 2p spectra of the Cu/CeO_2 catalyst sample. The main peak of Cu $2p_{3/2}$ appears at approximately 934.0 eV, with a satellite peak in the range of 938.1–946.2 eV, both of which are indicative of CuO [29]. In contrast, Cu^+ generally displays lower binding energy, and its distinctive peaks are not visible in the figure. This observation implies that Cu^+ species are minimally present, suggesting that copper predominantly exists as CuO on the catalyst surface. Figure 6d shows the Zr 3d spectra of the Zr/CeO_2 catalyst sample. The main peaks of Zr $3d_{5/2}$ are observed at 182.2 and 184.6 eV, with a binding energy difference of 2.4 eV. This is consistent with the standard spectrum for Zr 3d, a typical feature of ZrO_2, indicating that zirconium on the catalyst surface predominantly exists as ZrO_2, with few or no other zirconium oxides present.

The Ce 3d photoelectron spectra of all catalyst samples are shown in Fig. 7a, which all have similar peak patterns, and the two sets of spin–orbit coupling curves, Ce $3d_{5/2}$ and Ce $3d_{3/2}$, are denoted by the v-series and u-series, respectively, for ease of differentiation. Each M/CeO_2 catalyst sample Ce 3d spectral profile is characterized by eight distinct peaks arranged from low to high binding energy as follows: v(882.0 eV), v′(884.2 eV), v″(888.6 eV), v‴(898.2 eV), u(900.5 eV), u′(902.2 eV), u″(907.4 eV) and u‴(916.6 eV). Among them, two characteristic peaks, u′ and v′, are attributed to the characteristic peaks of Ce^{3+}, while the other six characteristic peaks are attributed to the characteristic peaks of Ce^{4+}. The molar ratio of Ce^{3+}/Ce^{4+} on the surface of the samples as determined from Ce 3d mapping of every catalyst is represented in Table 2. These ratios are derived from the area under the deconvolution integral peaks. In CeO_2 crystals, when Ce^{4+} is converted to Ce^{3+}, CeO_2 undergoes deoxygenation and generates oxygen vacancies to balance the charge, and this process can be expressed as $4Ce^{4+} + 2O_{lattice} \rightarrow 4Ce^{3+} + 2O_V + O_2$ (O lattice is lattice oxygen)[30]. Therefore, the amount of Ce^{3+} is directly related to oxygen vacancies, and more Ce^{3+} represents more lattice oxygen

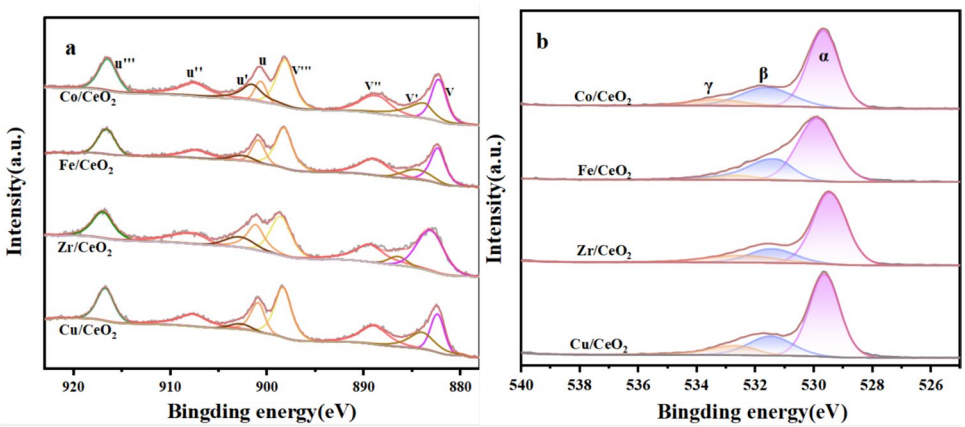

Fig. 7 XPS profiles of M/CeO_2: **a** Ce 3d, **b** O 1s

converted to oxygen vacancies, which is conducive to O_2 adsorption and activation, and thus improves the NH_3 oxidation capacity of the catalysts. The Ce^{3+}/Ce^{4+} molar ratios of each catalyst were ranked as follows: $Co/CeO_2 > Cu/CeO_2 > Fe/CeO_2 > Zr/CeO_2$, this is in perfect agreement with the ranking of ammonia-oxidizing activity above.

In the study of metal oxide catalysts, understanding how oxygen binds to the metal is crucial for assessing catalytic performance. O 1s spectroscopy is commonly used to identify oxygen types on catalyst surfaces. Figure 7b displays O 1s spectra for all samples, revealing binding energies of 529.7 eV for O_α, 531.6 eV for O_β, and 532.4 eV for O_γ. Among them, O_α is attributed to lattice oxygen (O^{2-}), and both O_β and $O_\gamma$are uniformly attributed to surface adsorbed oxygen O_A, but O_β contains more molecularly adsorbed oxygen and O^- species, while O_γ refers more to the oxygen in the hydroxyl group attached to the metal M (M-OH) [31, 32]. In general, surface-adsorbed oxygen O_A has better mobility [33], it has higher NH_3 oxidizing activity than lattice oxygen, and more O_A means better oxidizing activity. However, among the four M/CeO_2 prepared catalysts, as shown in Table 2, the relative content of surface adsorbed oxygen O_A ($O_\beta + O_\gamma$) is the same for each catalyst, i.e., the difference in oxidizing activity cannot be explained by O_A. However, it can also be found that the order of the size of the percentage of O_γ in the total O content of each catalyst corresponds to the order of the Ce^{3+}/Ce^{4+} concentration, indicating that for all the catalysts prepared in this paper, there is a synergistic effect between O_γ and Ce^{3+}/Ce^{4+}, with larger values corresponding to better NH_3 oxidation activity.

3.2.5 H_2-TPR Analysis

It is widely recognized by many scholars that the catalytic performance of catalysts is closely related to their reducing properties, and the H_2-TPR technique is usually employed to detect the reducing properties of catalysts. The H_2-TPR curves of different catalysts M/CeO_2 (M = Co, Cu, Fe, Zr) are shown in Fig. 8. In previous studies, the presence of a major reduction peak near 500 °C in pure CeO_2 was attributed to the reduction of surface oxygen [34–36]. The catalysts Co/CeO_2, Zr/CeO_2, and Fe/CeO_2 exhibited distinct reduction peaks of surface oxygen at temperatures of 472.2, 519.2, and 595.8 °C, respectively. These variations in peak temperatures, characterized by both decreasing and increasing trends around the peak centers, are indicative of the interactions occurring between the CeO_2 support and the Co, Zr, and Fe metals. For the Co/CeO_2 sample, the peaks observed at 264.5, 312.2, and 472.2 °C are associated with the successive reduction of Co^{3+} to Co^{2+} and then to Co^0. The peak at a higher temperature (472.2 °C) suggests the presence of more stable cobalt oxides or interactions between cobalt and ceria [37]. In the Fe/CeO_2 sample, reduction peaks

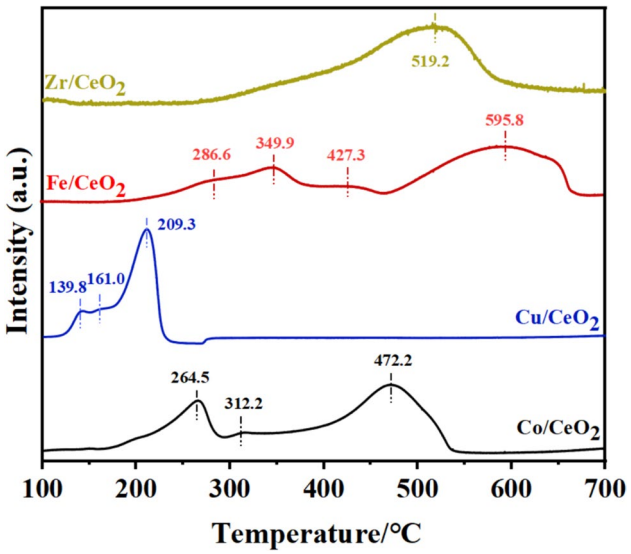

Fig. 8 H_2-TPR profiles of M/CeO_2 catalysts

were identified at 286.6 and 349.9 °C, corresponding to the reduction of Fe^{3+} to Fe^{2+} and Fe^{2+} to Fe^0, respectively [38]. Additional peaks at 427.3 and 595.8 °C are likely attributed to the formation of complex iron oxides and strong interactions with ceria [38]. The Zr/CeO_2 sample exhibited a peak at 519.2 °C, which is indicative of ceria reduction facilitated by the presence of zirconium, highlighting significant metal-support interactions [39]. For Cu/CeO_2, the reduction peak of surface oxygen typically observed around 500 °C is absent, which can be attributed to the strong metal-oxide supported interaction (SMSI) between CuO and CeO_2 [36]. Below 300 °C, three distinct reduction peaks were observed at around 139.8, 161.0 and 209.3 °C indicating the presence of three distinct Cu species on the Cu/CeO_2 catalyst surface. These species are identified, in decreasing order, as highly dispersed CuO_X, the Cu–O–Ce structure, and the crystalline state of the CuO [40]. For the Fe/CeO_2 catalyst, three additional reduction peaks at temperatures 286.6, 349.9, and 427.3 °C correspond to the sequential reduction of FeO_X species. For Co/CeO_2, two distinct peaks observed around 264.5 and 312.2 °C were associated with the reduction of CoO_X.

3.2.6 Raman Analysis

To study the structural information of M/CeO_2 (M = Co, Cu, Fe, Zr) catalysts in more detail, Raman spectroscopy was used in this study for each catalyst sample. In general, it provides specific information about oxygen vacancies and oxygen sublattice distortions [41]. Figure 9 demonstrates the Raman spectra of each catalyst sample in this study. They all have a distinct Raman characteristic peak near 465 cm^{-1}, which is attributed to the F_{2g} peak of fluorite-structured CeO_2 and is

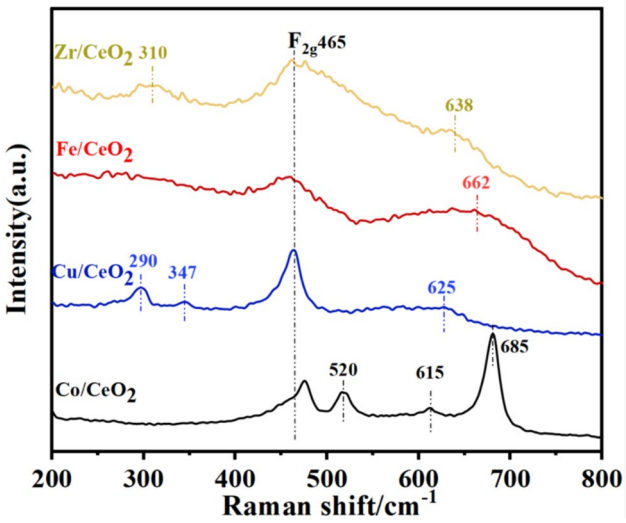

Fig. 9 Raman profiles of M/CeO_2 catalysts

caused by the symmetric stretching of the Ce–O vibrational unit in the octet of coordination [42]. In pure CeO_2, the F_{2g} peak is usually a sharp peak located at 465 cm^{-1}. As shown in Fig. 9, the F_{2g} peaks of each M/CeO_2 (M = Co, Cu, Fe, Zr) catalyst sample showed some degree of positional shift, which was attributed to the slight deformation of the CeO_2 lattice induced by the participation of M^{x+} (M = Co, Cu, Fe, Zr) ions [43]. In addition, the different degrees of broadening and enlargement of the F_{2g} peaks can be assumed to be related to the increase in the concentration of oxygen vacancies since the F_{2g} peaks are very sensitive to the disorder of the oxygen sublattice. Therefore, the changes in Raman F_{2g} peak shape and peak position of the Raman F_{2g} peaks of each catalyst sample compared to the Raman F_{2g} peaks of pure CeO_2 indicate the existence of strong interactions between each M metal and Ce. For the Co/CeO_2 sample, additional Raman peaks at 520, 615, and 685 cm^{-1}, respectively, are attributed to Co_3O_4 [44]. For the Cu/CeO_2 sample, three additional Raman peaks at 290, 347, and 625 cm^{-1} were attributed to CuO. For the Fe/CeO_2 sample, the Raman peak at 662 cm^{-1} is attributed to Fe_2O_3. For the Zr/CeO_2 sample, the Raman peaks appearing at 310 and 638 cm^{-1} are attributed to ZrO_2. The appearance of new Raman peaks in all the above catalyst samples suggests that some MO_x material is still present on the surface of the prepared catalyst samples despite the incorporation of M-metals (M = Co, Cu, Fe, Zr) into the CeO_2-based catalysts to form a Ce–O-M solid solution.

4 Conclusions

In this study, a series of CeO_2-based catalysts denoted as M/CeO_2 (M = Co, Cu, Fe, Zr) catalysts, were synthesized using the citric acid sol–gel method. These catalysts were evaluated for NH_3-SCO performance on a simulated gas experimental platform. To elucidate the relationship between the physicochemical properties and catalytic performance, comprehensive characterization techniques including BET, XRD, and XPS were employed. The key findings are summarized as follows:

1. In terms of ammonia-oxidizing activity, the Co/CeO_2 catalyst demonstrated superior performance, with a T_{90} as low as 239.2 °C. The catalysts were ranked based on their ammonia oxidation activities as follows $Co/CeO_2 > Cu/CeO_2 > Fe/CeO_2 > Zr/CeO_2$. Conversely, N_2 selectivity followed an inverse trend: $Co/CeO_2 < Cu/CeO_2 < Fe/CeO_2 < Zr/CeO_2$, indicating a trade-off between ammonia oxidation activity and N_2 selectivity. Considering both metrics, the Cu/CeO_2 catalyst emerged as the best catalytic performance, which offers an optimal balance between high ammonia oxidation activity and favorable N_2 selectivity.
2. Structural characterization via SEM, BET, and XRD confirmed that CeO_2 was the predominant phase in each catalyst, exhibiting a cubic fluorite structure, consistent with the synthesis approach. Among the four catalysts with the same mesoporous structure, Co/CeO_2 and Cu/CeO_2 had the largest specific surface area (77.37 m^2g^{-1}) and the smallest pore volume (0.13 cm^3g^{-1}), respectively, which may be associated to their possessed better ammonia oxidation activity.
3. Further insights were gained from XPS, H_2-TPR, and Raman spectroscopy. XPS analysis showed that the O_γ content in the surface adsorbed oxygen O_A had a certain synergistic effect with the Ce^{3+}/Ce^{4+} value, with high ratios correlating, with the improved ammonia oxidation activity. H_2-TPR results showed that the incorporation of Co, Zr, Fe, and CeO_2 shifted the surface oxygen reduction peak of pure CeO_2 near 500 °C. The Co/CeO_2 peak position shifted toward the low temperature indicating enhanced surface oxygen activity and improved reduction performance. The Cu/CeO_2 catalyst displayed a complete disappearance of the reduction peak suggesting a strong interaction between Cu and Ce. Raman results confirmed the formation of Ce–O–M solid solution in all M/CeO_2 catalysts, though some MO_X material remained on the surface of the samples.

Acknowledgements We would like to acknowledge the National Natural Science Foundation of China (52076104) for the financial support of this paper.

Declarations

Conflicts of Interest There are no conflicts of interest to declare.

References

1. Gu B, Zhang L, Van Dingenen R et al (2021) Abating ammonia is more cost-effective than nitrogen oxides for mitigating $PM_{2.5}$ air pollution. Science 374:758–762
2. Wen Y, Zhang S, Wu Y et al (2023) Vehicular ammonia emissions: an underappreciated emission source in densely populated areas. Atmos Chem Phys 23:3819–3828
3. Zhang M, Wang H, Fan B et al (2024) Progress of ammonia selective catalytic oxidation research and performance improvement strategy. J Environ Chem Eng 12:112306
4. Feng P, Lee M, Wang D et al (2023) Ammonia thermal decomposition on quartz and stainless steel walls. Int J Hydr Energy 48:29209–29219
5. Valenzuela-Heredia D, Aroca G (2023) Methane biofiltration for the treatment of a simulated diluted biogas emission containing ammonia and hydrogen sulfide. Chem Eng J 469:143704
6. Lendzion-Bielun Z, Narkiewicz U, Arabczyk W (2013) Cobalt-based catalysts for ammonia decomposition. Materials (Basel, Switzerland) 6:2400–2409
7. Bruno JC, Ortega-López V, Coronas A (2009) Integration of absorption cooling systems into micro gas turbine trigeneration systems using biogas: case study of a sewage treatment plant. Appl Energy 86:837–847
8. Qiu Y, Li X, Zhang Y et al (2019) Various metals (Ce, In, La, and Fe) promoted Pt/Sn-SBA-15 as highly stable catalysts for propane dehydrogenation. Ind Eng Chem Res 58:10804–10818
9. Jabłońska M, Palkovits R (2016) Copper based catalysts for the selective ammonia oxidation into nitrogen and water vapour—recent trends and open challenges. Appl Catal B 181:332–351
10. Scheuer A, Hauptmann W, Drochner A et al (2012) Dual layer automotive ammonia oxidation catalysts: experiments and computer simulation. Appl Catal B 111–112:445–455
11. Yao P, Li J, Pei M et al (2024) Engineering a PtCu alloy to improve N_2 selectivity of NH_3-SCO over the Pt/SSZ-13 catalyst. ACS Appl Mater Interfaces 16:14694–14703
12. Kim M-S, Lee D-W, Chung S-H et al (2012) Oxidation of ammonia to nitrogen over Pt/Fe/ZSM-5 catalyst: influence of catalyst support on the low temperature activity. J Hazard Mater 237–238:153–160
13. Hung C-M (2010) Cordierite-supported Pt–Pd–Rh ternary composite for selective catalytic oxidation of ammonia. Powder Technol 200:78–83
14. Qu Z, Wang H, Wang S et al (2014) Role of the support on the behavior of Ag-based catalysts for NH_3 selective catalytic oxidation (NH_3-SCO). Appl Surf Sci 316:373–379
15. Chen W, Qu Z, Huang W et al (2016) Novel effect of SO_2 on selective catalytic oxidation of slip ammonia from coal-fired flue gas over IrO_2 modified Ce–Zr solid solution and the mechanism investigation. Fuel 166:179–187
16. Li X, Chen J, Lu C et al (2021) Performance of Mo modified γ-Fe_2O_3 catalyst for selective catalytic reduction of NOx with ammonia: presence of arsenic in flue gas. Fuel 294:120552
17. Su X, Gao X, Yu X-Y et al (2024) Design of Cu-based bimetals for ammonia catalytic combustion via DFT-based microkinetic modeling. J Catal 429:115264
18. Kong X, Li Z, Shao Y et al (2022) Modulate the superficial structure of $La_2Ce_2O_7$ catalyst with anchoring CuOx species for the selective catalytic oxidation of NH_3. J Mater Sci Technol 111:1–8
19. Marchuk V, Huang X, Murzin V et al (2022) Operando QEXAFS study of Pt–Fe ammonia slip catalysts during realistic driving cycles. Top Catal 66:825–838
20. Liu W, Long Y, Liu S et al (2023) Ce–Ti catalysts modified with copper and vanadium to effectively remove slip NH_3 and NOx from coal-fired plants. J Rare Earths 41:1022–1030
21. Liu Z, Wu M, Ma J (2022) Ni–Cu–Co grid-like hydroxyl oxide ammonia oxidation reaction catalyst supported on carbon nanotubes. Energy Fuels 36:10339–10345
22. Chen X, Yang J, Liu Z et al (2023) Origin of ammonia selective oxidation activity of $SmMn_2O_5$ mullite: a first-principles-based microkinetic study. ACS Appl Mater Interfaces 15:736–750
23. Wang Z, Qu Z, Quan X et al (2012) Selective catalytic oxidation of ammonia to nitrogen over ceria–zirconia mixed oxides. Appl Catal A 411:131–138
24. Liao DL, Badour CA, Liao BQ (2008) Preparation of nanosized TiO_2/ZnO composite catalyst and its photocatalytic activity for degradation of methyl orange. J Photochem Photobiol, A 194:11–19
25. Qu Z, Gao K, Fu Q et al (2014) Low-temperature catalytic oxidation of toluene over nanocrystal-like Mn–Co oxides prepared by two-step hydrothermal method. Catal Commun 52:31–35
26. Chen Y, Zhao S, Liu Z (2015) Influence of the synergistic effect between Co–N–C and ceria on the catalytic performance for selective oxidation of ethylbenzene. Phys Chem Chem Phys 17:14012–14020
27. Li J, Xiong S, Li X et al (2012) Spinel $Mn_{1.5}Co_{1.5}O_4$ core–shell microspheres as Li-ion battery anode materials with a long cycle life and high capacity. J Mater Chem 22:23254–23259
28. Wang X, Zhang L, Wu S et al (2016) Promotional effect of Ce on iron-based catalysts for selective catalytic reduction of NO with NH_3. Catalysts 6:112
29. Qi L, Yu Q, Dai Y et al (2012) Influence of cerium precursors on the structure and reducibility of mesoporous CuO-CeO_2 catalysts for CO oxidation. Appl Catal B 119–120:308–320
30. Montini T, Melchionna M, Monai M et al (2016) Fundamentals and catalytic applications of CeO_2-based materials. Chem Soc Rev 116:5987–6041
31. Santos VP, Pereira MFR, Órfão JJM et al (2010) The role of lattice oxygen on the activity of manganese oxides towards the oxidation of volatile organic compounds. Appl Catal B 99:353–363
32. Jirátová K, Mikulová J, Klempa J et al (2009) Modification of Co–Mn–Al mixed oxide with potassium and its effect on deep oxidation of VOC. Appl Catal A 361:106–116
33. Kropp T, Paier J, Sauer J (2017) Oxidative dehydrogenation of methanol at ceria-supported vanadia oligomers. J Catal 352:382–387
34. Fally F, Perrichon V, Vidal H et al (2000) Modification of the oxygen storage capacity of CeO_2–ZrO_2 mixed oxides after redox cycling aging. Catal Today 59:373–386
35. Djinović P, Batista J, Pintar A (2008) Calcination temperature and CuO loading dependence on CuO-CeO_2 catalyst activity for water-gas shift reaction. Appl Catal A 347:23–33
36. Muroyama H, Hano S, Matsui T et al (2010) Catalytic soot combustion over CeO_2-based oxides. Catal Today 153:133–135
37. Choi T-Y, Kim H-M, Park M-J et al (2022) Effect of ZrO_2 on the performance of Co–CeO_2 catalysts for hydrogen production from waste-derived synthesis gas using high-temperature water gas shift reaction. Int J Hydr Energy 47:14294–14303

38. Feng L, Xing X, Du Y et al (2023) Low-temperature CO oxidation over CuO–CeO_2/Fe_2O_3 catalyst: effect of $KMnO_4$ modification. Metals 13:186
39. Hu X, Mao D, Yu J et al (2023) Low-temperature CO oxidation on CuO–CeO_2–ZrO_2 catalysts prepared by a facile surfactant-assisted grinding method. Fuel 340:127529
40. Wang F, Büchel R, Savitsky A et al (2016) In situ EPR study of the redox properties of CuO–CeO_2 catalysts for preferential CO oxidation (PROX). ACS Catal 6:3520–3530
41. Li L, Xue S, Wei M et al (2022) Ultrafine Pd species anchored on porous CeO2 nanobundles as a highly efficient catalyst for methane oxidation. Appl Surf Sci 599:153909
42. Li X, Lu X, Meng Y et al (2013) Facile synthesis and catalytic oxidation property of palygorskite/mesocrystalline $Ce_{1-x}Mn_xO_2$ nanocomposites. J Alloy Compd 562:56–63
43. Wu X, Liu S, Weng D et al (2011) MnOx–CeO2–Al2O3 mixed oxides for soot oxidation: activity and thermal stability. J Hazard Mater 187:283–290
44. Liu Q, Wang L-C, Chen M et al (2009) Dry citrate-precursor synthesized nanocrystalline cobalt oxide as highly active catalyst for total oxidation of propane. J Catal 263:104–113

Authors and Affiliations

Longwei Cheng[1] · Pan Wang[1] · Quanxin Ye[1] · Hongyu Zhao[1] · Sheikh Muhammad Farhan[1] · Tong Yan[1] · Hailin Zhao[2]

✉ Pan Wang
wangpan@ujs.edu.cn

[1] School of Automotive and Traffic Engineering, Jiangsu University, Zhenjiang 212013, China

[2] Kailong Lanfeng New Material Technology Company, Zhenjiang 212000, China